Journal of The Electrochemical Society, **148** (4) G207-G214 (2001)
0013-4651/2001/148(4)/G207/8/$7.00 © The Electrochemical Society, Inc.

Three-Dimensional Chemical Mechanical Planarization Slurry Flow Model Based on Lubrication Theory

Dipto G. Thakurta,[a,b] Christopher L. Borst,[a,b] Donald W. Schwendeman,[c] Ronald J. Gutmann,[b,d] and William N. Gill[a,b,z]

[a]*Department of Chemical Engineering,* [b]*Center for Integrated Electronics and Electronic Manufacturing,* [c]*Department of Mathematical Sciences,* [d]*Department of Electrical, Computer and Systems Engineering, Rensselaer Polytechnic Institute, Troy, New York 12180, USA*

A three-dimensional chemical mechanical planarization slurry flow model based upon lubrication theory is developed, utilizing a generalized Reynolds equation that includes pad porosity and bending. The model is used to calculate slurry film thickness and slurry velocity distributions between the wafer and pad, with the minimum slurry film thickness determining the degree of contact between the wafer and pad. The dependence of the removal rate of copper films as a function of applied pressure and velocity agrees well with model predictions. The minimum slurry film thickness is examined over a range of input variables, namely, applied pressure, wafer-pad velocity, wafer radius and curvature, slurry viscosity, and pad porosity and compressibility.
 [DOI: 10.1149/1.1355691]

Manuscript received February 14, 2000.

Over the last decade, chemical mechanical planarization (CMP) has become a key technology for subhalf-micrometer integrated circuit (IC) device manufacturing.[1] CMP has been widely used for planarization of interlevel dielectric (ILD), shallow trench isolation (STI), and the Damascene metallization process.[2-5] During the CMP process, a wafer is rotated on its axis while being pressed face down by a carrier against a rotating polish pad. A polishing slurry containing chemical reagents and abrasive particles is delivered on top of the pad. The slurry forms a thin lubricating film between the wafer and pad. Both chemical and mechanical mechanisms have been identified as synergistic contributing factors to the overall material removal phenomenon.[6] In spite of extensive use of the CMP process, many aspects of CMP are not well understood. Hence, physics-based modeling is useful in providing fundamental insight, optimization of the process, and performing sensitivity analyses of operating parameters.[7] Several CMP models have been published in the literature, with Nanz and Camilletti[8] presenting a good review of the existing models up to 1995. A very recent article by Subramanian *et al.*[9] also presents a comprehensive summary of published CMP models. In our paper, we develop a three-dimensional (3-D) wafer-scale CMP slurry flow model based on a generalized Reynolds equation which can predict the thickness of the slurry film formed between the wafer and pad.

In an earlier paper,[10] we identified two different regimes of CMP operation depending upon the slurry film thickness, namely, the lubrication and the contact regimes. In the lubrication regime, a thicker slurry film ($\gtrsim$20 μm) separates the wafer and pad. The fluid pressure developed in this slurry film supports the load applied to the wafer carrier. The fluid shear stress and chemical action at the wafer surface cause material removal.[11-13] In the contact regime, the wafer-pad solid to solid contact pressure supports the load primarily. Contact stresses at the wafer surface lead to higher polish rates in the contact regime. Although higher removal rates are achieved in the contact regime, the lubrication regime is more applicable for polishing softer materials, *e.g.*, polymer ILDs,[14] which cannot sustain high contact stresses. Polish characteristics such as surface finish, nonuniformity, erosion, and dishing also depend on the CMP regime.

The degree of wafer-to-pad contact is determined by the thickness of slurry film between the wafer and pad.[15] If the slurry film thickness is greater than the average height of pad asperities ($\sim$20 μm[16-18]), then the operation is considered to be in the lubrication regime. If the computed film thickness is less than the height of the pad asperities, then contact regime operation is more likely.[10] In this paper, we examine the effect of all operating parameters on film thickness using the slurry flow model.

The distinction between the two regimes is made for the purposes of modeling. In between the lubrication and contact regimes, which are on either sides of the spectrum, there is a mixed regime containing features of both regimes. In this paper, we do not consider contact between wafer and pad and hence we essentially model the lubrication regime.

The first published work on wafer-scale slurry flow modeling is by Runnels and Eyman.[11] They solved the steady-state 3-D Navier-Stokes equations numerically using a finite element scheme in the region between the pad and wafer. The angle of attack of the wafer is adjusted in an iterative manner to obtain a stable position of the wafer which balances the moment about the gimbaling point. They studied the effect of wafer curvature, slurry viscosity, and wafer and pad rotation speeds on the thickness of the slurry film. Yu *et al.*[15] and Rogers *et al.*[19] have presented 2-D slurry flow models also based on the solution of the Navier-Stokes equations.

Solving the Navier-Stokes equations, especially in 3-D, is expensive computationally. Considerable simplifications for solving the slurry flow may be achieved if one recognizes that the reduced Reynolds number[13]

$$Re^* = \frac{\rho U R_1}{\mu}\left(\frac{\overline{h}}{R_1}\right)^2 \qquad [1]$$

is small where ρ and μ are the slurry density and viscosity, respectively, U is the relative velocity between the wafer and pad, and R_1 is the wafer radius. A typical film thickness, $\overline{h}$, is of the order of micrometers which results in a value of Re^* in the range of 10^{-2} to 10^{-3}; therefore, the lubrication approximations used in the theory of slider bearings are valid. 2-D slurry flow models by Sundararajan *et al.*,[13] Tichy *et al.*,[20] and Thakurta *et al.*[10] are all based on lubrication theory. In this article, we extend our previous 2-D work[10] to 3-D. A comparison of the 3-D results with previous 2-D work shows qualitative agreement, but reveals significant quantitative differences. We believe that the 3-D model predictions are more accurate because the 3-D formulation considers an actual tool geometry and explicitly includes the effects of wafer and pad rotation.

A similar 3-D model also based on lubrication theory has been developed independently and simultaneously by Jiang and Shankar.[21] They obtain the slurry pressure and velocity distributions for flow with pad asperity/wafer contact by using a statistical averaging approach analogous to the Patir and Cheng[22] model for rough bearing lubrication. First, the flow is solved numerically locally in an element with statistically equivalent rough surfaces. These local

[z] E-mail: gillw@rpi.edu

flow patterns are averaged over the volume to provide flow-factors which are then included in the wafer-scale lubrication model.

CMP pads, which are typically made of polyurethane, are porous and bend under the applied pressure. Both pad bending and porosity affect the flow hydrodynamics, slurry film thickness, and angle of attack of the wafer. The shape of the wafer/pad gap changes due to pad bending. At the same time, pad porosity causes a small amount of the slurry to leak or seep into the pad underneath the wafer. The current model includes the important effects of pad porosity and bending but does not incorporate the effect of pad roughness. Since the focus of this work is a detailed study of the lubrication regime of CMP, neglecting pad roughness is reasonable.

In this paper, we formulate the lubrication equations for our CMP configuration, study the effect of all input parameters on slurry film thickness, and correlate the results with experimental data. The input parameters for the model include wafer and pad rotation speeds, applied pressure, wafer diameter, wafer curvature, and pad porosity and compressibility. A dimensional analysis is used to identify key dimensionless groups of input parameters. The model also computes 3-D slurry velocity fields between the wafer and pad which could be used in CMP mass transport calculations[13] and to study slurry flow patterns.

Copper CMP experiments were performed to relate the removal rate with two of the most important input parameters, namely, the applied pressure and the wafer and pad angular velocities. The experiments were designed using our model predictions to correlate removal rate data for different slurry and pad combinations over a wide range of pressure and velocity. A strong correlation is found between the measured removal rate and the predicted wafer/pad separation, which supports the validity of our model.

Slurry Flow Model Development

Figure 1 illustrates the 3-D lubrication model for slurry flow including the arrangement and geometry of the wafer and pad. The wafer radius is R_1 and the distance between the centers of the wafer and pad is R_2. The wafer and pad rotate about their respective centers with angular speeds ω_1 and ω_2, respectively. The wafer is held by a gimbaling mechanism which pivots to a stable configuration with an assumed zero moment of torque about the x and y axes.[11] The coordinate system is fixed in space with the origin at the undeformed pad surface directly below the center of the wafer. Both Cartesian (x, y, z) and cylindrical (r, θ, z) coordinates will be used interchangeably, for convenience. For the cylindrical system, $\theta = 0$ is oriented along the x axis and θ increases in the counterclockwise direction as shown in Fig. 1a.

The wafer height is given by $z = h(x,y)$ measured relative to an undeformed pad surface (the x-y plane) and includes a global curvature and angles of attack. A global convex curvature is often imposed by the shape of the wafer backing film[23] and/or by applying back pressure to help offset excessive material removal at the edges. The curvature is represented in terms of the protrusion at the center of the wafer, also known as the wafer dome height.[11] The wafer dome height is denoted by δ_0 and is of the order of 10 μm for an 8 in. diam wafer. (The curvature shown in Fig. 1b is exaggerated for the purpose of illustration.) The wafer surface is taken to be

$$h(x,y) = h_0 + S_x\left[\frac{x}{R_1}\right] + S_y\left[\frac{y}{R_1}\right] + \delta_0\left[\frac{x^2 + y^2}{R_1^2}\right] \qquad [2]$$

where h_0 is the wafer height at the origin, and S_x and S_y are slopes associated with the angles of attack in the x and y directions, respectively. These three unknown parameters are adjusted to satisfy the load and moment constraints (discussed later). Values for R_1, R_2, and δ_0 are considered to be known.

Due to the thin gap between the pad and wafer, a significant lubricating pressure $P_f(x,y)$ develops in the slurry film which supports the constant downward applied pressure P_{app} to the wafer and causes a deflection of the pad given by $z = s(x,y)$. (All pressures are measured relative to atmospheric pressure.) It is assumed that the pad behaves, to a first approximation, as a linear spring so that the fluid pressure $P_f(x,y)$ and pad deflection $s(x,y)$ are related locally by Hooke's law

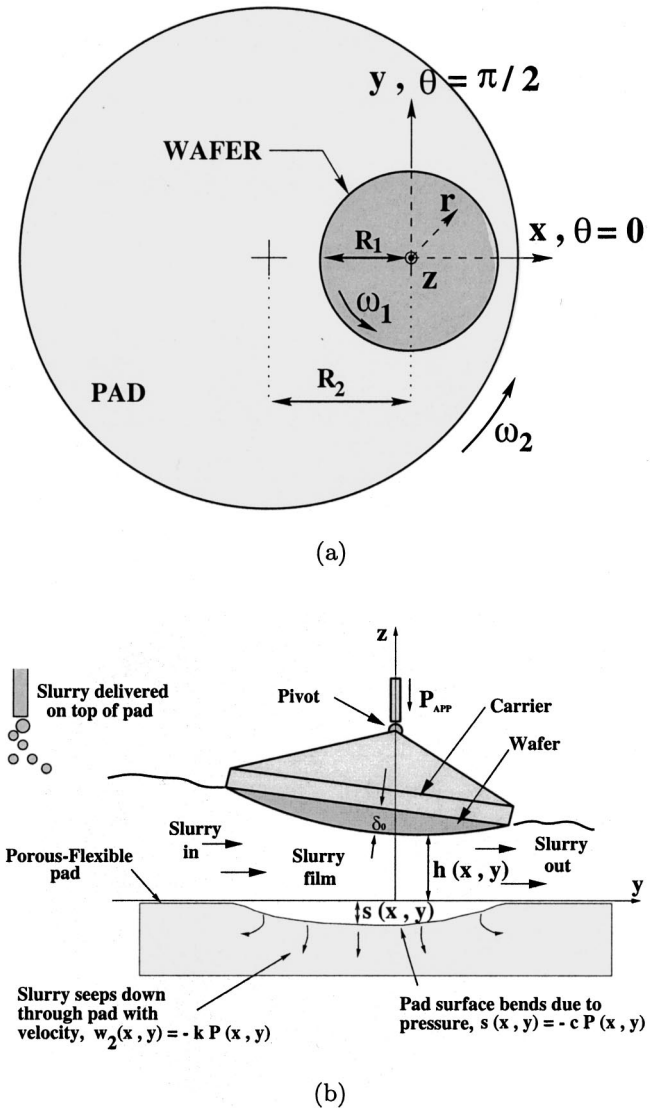

Figure 1. (a) Schematic top view of CMP tool showing pad and wafer positions. (b) Schematic side view of 3-D lubrication model.

$$s(x,y) = -cP_f(x,y) \qquad [3]$$

where the spring constant c measures the compressibility of the pad. This model neglects bending moments in the pad which is reasonable except possibly for a small region near the edge of the pad.[24] The minus sign in the model indicates that a positive pressure results in a downward pad deflection when $c > 0$.

In the gap between the pad and wafer, the x, y, and z components of the slurry velocity are given by u, v, and w, respectively. (Correspondingly, let v_r, v_θ, and w denote the r, θ, and z components of velocities, respectively, in the cylindrical coordinate system.) At the wafer surface, the slurry velocity satisfies the no-slip and no-flow penetration conditions so that

$$u_1 \equiv u(x,y,h) = -\omega_1 y \quad v_1 \equiv v(x,y,h) = \omega_1 x \qquad [4]$$

and

$$w_1 \equiv w(x,y,h) \simeq \omega_1\left(x\frac{S_y}{R_1} - y\frac{S_x}{R_1}\right) \quad [5]$$

The velocity components at the wafer surface given above are obtained from the cross product $\omega_1\hat{n} \times \mathbf{x}$, where $\hat{n} = -\nabla h(0,0)/|\nabla h(0,0)|$ is the unit vector normal to the wafer surface at $x = y = 0$ (the axis of rotation of wafer) and $\mathbf{x} = x\hat{i} + y\hat{j} + h\hat{k}$ is any point on the wafer surface, with $\hat{i}$, $\hat{j}$, and $\hat{k}$ denoting unit vectors in the x, y, and z directions, respectively. In a similar manner, pad velocity components may also be found. At the pad surface, a no-slip boundary condition is assumed so that

$$u_2 \equiv u(x,y,s) = -\omega_2 y$$

and

$$v_2 \equiv v(x,y,s) = \omega_2(x + R_2) \quad [6]$$

(Subscripts 1 and 2 used with u, v, and w denote velocities at the wafer and pad surface, respectively.) Pad porosity causes a certain amount of the slurry to seep into the pad underneath the wafer. Darcy's model is used to describe the effect of porosity of the pad. Hence the z component of the velocity at the pad is determined by the fluid pressure and porosity, k, of the pad

$$w_2 \equiv w(x,y,s) = -kP_f(x,y) \quad [7]$$

where the minus sign indicates that the seepage velocity is in the negative z direction when $k > 0$.

The flow of the slurry fluid is assumed incompressible and Newtonian. The equation of continuity is given by

$$\nabla \cdot \mathbf{u} + \frac{\partial w}{\partial z} = 0 \quad [8]$$

where $\mathbf{u} = u\hat{i} + v\hat{j} = \langle u,v\rangle$ is used for abbreviation. Lubrication approximations to the Navier-Stokes equation are used as the reduced Reynolds number (see Eq. 1) is small. Hence, the convection terms are dropped in the horizontal momentum equations

$$\nabla P_f = \mu\frac{\partial^2 \mathbf{u}}{\partial z^2} \quad [9]$$

and the momentum equation in the z direction reduces to

$$\frac{\partial P_f}{\partial z} = 0 \quad [10]$$

Equation 10 implies that the fluid pressure does not vary in the z direction as the thickness of the gap is much smaller than the wafer radius. The z independence was tacitly assumed in Eq. 3 and 7. After integrating the horizontal momentum equation (Eq. 9) twice with respect to z and using the known u velocities (Eq. 4 and 6) at the wafer and pad surface to evaluate the two constants of integration, we obtain

$$\mathbf{u} = -\frac{1}{2\mu}\nabla P_f(h - z)(s + z) + \frac{\mathbf{u}_1 - \mathbf{u}_2}{h - s}z + \frac{\mathbf{u}_2 h - \mathbf{u}_1 s}{h - s} \quad [11]$$

where $\mathbf{u}_1 = \langle u_1,v_1\rangle$ and $\mathbf{u}_2 = \langle u_2,v_2\rangle$. The continuity equation (Eq. 8) is integrated from $z = s$ to $z = h$ to give

$$\int_s^h \nabla \cdot \mathbf{u}dz + \int_s^h \frac{\partial w}{\partial z}dz = 0 \quad [12]$$

The first integral is evaluated using Leibnitz's rule and by substituting the value of u from Eq. 11, while the second integral reduces to $w_1 - w_2$. The result is the generalized Reynolds equation (Eq. 13), which holds for arbitrary wafer surface h and pad surface s, and also includes effects of pad bending and porosity

$$-\frac{1}{12\mu}\nabla \cdot \{(h - s)^3\nabla P_f\} + \frac{(h - s)}{2}\nabla \cdot (\mathbf{u}_1 + \mathbf{u}_2) + \frac{(\nabla h + \nabla s)}{2} \cdot (\mathbf{u}_2 - \mathbf{u}_1) + w_1 - w_2 = 0 \quad [13]$$

The above equation is solved for P_f on the domain $0 < r < R_1$, $0 < \theta < 2\pi$ subject to the boundary condition

$$P_f(R_1,\theta) = 0 \quad [14]$$

indicating atmospheric pressure at the wafer edge. Hence, using lubrication theory, one reduces a four-variable 3-D problem of solving u, v, w, and P_f to a one-variable 2-D problem of solving P_f. Equation 13 can be expressed in either Cartesian or cylindrical coordinates. Solution in a cylindrical system is easier to incorporate the boundary condition in Eq. 14 and the integral constraints given below. In Eq. 13, $\mathbf{u}_1$, $\mathbf{u}_2$, w_1, w_2, h, and s are substituted from Eq. 4, 6, 5, 7, 2, and 3, respectively. The unknown parameters h_0, S_x, and S_y in the expression of h are adjusted to balance the applied pressure and to satisfy zero moments about $x = 0$ and $y = 0$. These three constraints are given in terms of the pressure by

$$\frac{1}{\pi R_1^2}\int_0^{2\pi}\int_0^{R_1} P_f(r,\theta)rdrd\theta = P_{app} \quad [15]$$

$$\int_0^{2\pi}\int_0^{R_1} P_f(r,\theta)r\sin(\theta)rdrd\theta = M_{fx} = 0 \quad [16]$$

and

$$\int_0^{2\pi}\int_0^{R_1} P_f(r,\theta)r\cos(\theta)rdrd\theta = M_{fy} = 0 \quad [17]$$

respectively.

Equation 13 and the boundary condition in Eq. 14 are solved numerically using a finite difference formulation and a provisional choice for h_0, S_x, and S_y which results in a discrete set of values for P_f on a grid. Newton's method of iteration is used to adjust h_0, S_x, and S_y until the load (Eq. 15) and moment (Eq. 16 and 17) constraints are satisfied. The solution set $\{P_f,h_0,S_x,S_y\}$ is a function of the known input parameters listed in Table I. [Rotations per minute (rpm) is used as units for angular velocities of the pad and wafer. The units for c and k follow from their definitions in Eq. 3 and 7, respectively.] A dimensional analysis of the Reynolds equation reveals that the solution set is a function of the following five dimensionless groups

Table I. Tool, wafer, pad, and slurry input parameters for model.

Input parameter	Symbol	Unit
Applied pressure	P_{app}	kPa
Wafer angular speed	ω_1	rpm
Pad angular speed	ω_2	rpm
Radius of wafer	R_1	inch
Distance between wafer and pad centers	R_2	inch
Wafer dome height	δ_0	μm
Slurry viscosity	μ	Pa s
Pad porosity	k	m s^{-1} Pa^{-1}
Pad compressibility	c	m Pa^{-1}

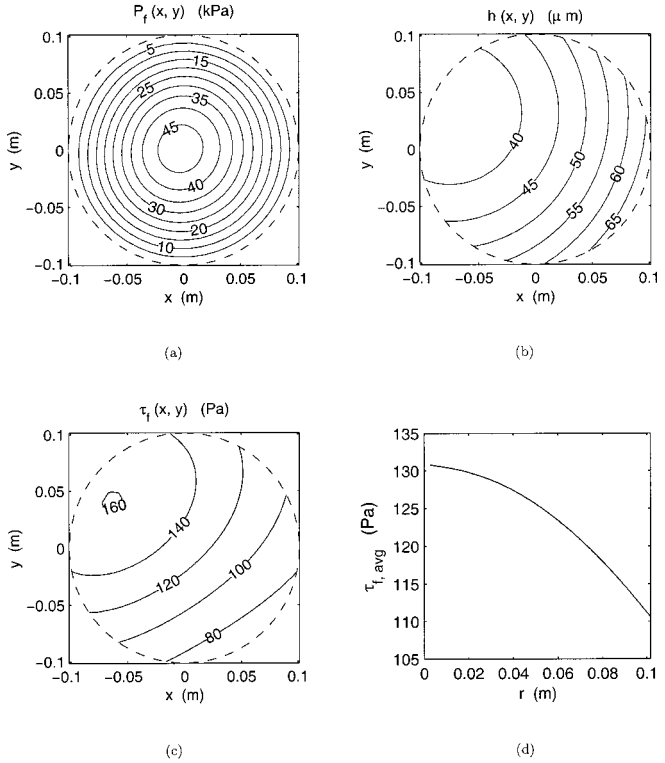

Figure 2. Computed slurry (a) pressure and (b) thickness distributions under wafer. (Wafer edge shown by broken line.) (c) Fluid shear stress at wafer surface. (d) Plot of shear stress averaged over θ against wafer radial position *r*. Input parameters used: $P_{app} = 21$ kPa, $\omega_1 = \omega_2 = 60$ rpm, $R_1 = 4$ in., $R_2 = 7$ in., $\delta_0 = 10$ μm, $\mu = 0.005$ Pa s, $c = 0$ m Pa^{-1}, and $k = 0$ m s^{-1} Pa^{-1}.

$$\left\{\frac{\delta_0}{z_0},\ \frac{R_1}{R_2},\ \frac{\omega_1}{\omega_2},\ \frac{kP_{app}}{\omega_2 z_0},\ \frac{cP_{app}}{z_0}\right\} \qquad [18]$$

where z_0 is a length scale in the z direction given by

$$z_0 = \left\{\frac{\mu\omega_2 R_2 R_1}{P_{app}}\right\}^{1/2} \qquad [19]$$

The dimensional analysis reduces the number of parameters and provides a means to represent computed data more compactly.

Once the pressure distribution and the parameters h_0, S_x, and S_y are found, the slurry thickness and velocity distributions can be computed using Eq. 2 and 11, respectively. The z component of velocity follows from the equation of continuity and the boundary condition given by Eq. 5 or 7. In the next section, we present solutions for a sample case and study the effect of the input parameters on film thickness.

Model Results

Key concepts and comparison with previous models.—As described in the previous section, the slurry pressure, thickness, shear stress, and velocity distributions can be computed once the Reynolds equation is solved. Solutions are presented for a typical sample case with $P_{app} = 21$ kPa and $\omega_1 = \omega_2 = 60$ rpm in Fig. 2, 3, and 4; the input parameters used for the computations are listed in the caption of Fig. 2. The computed slurry pressure $P_f(x,y)$ and thickness $h(x,y)$ distributions are shown in Fig. 2a and b, respectively. The slurry fluid pressure increases from atmospheric pressure (0 Pa) at the wafer edge to a maximum of 47 kPa near the wafer center. As there is no contact between the wafer and pad, P_f developed in the slurry film completely supports the applied pressure of 21 kPa. The pressure distribution resembles a paraboloid and is approximately symmetric indicating that the constraints $M_{fx} = M_{fy} = 0$ have been satisfied.

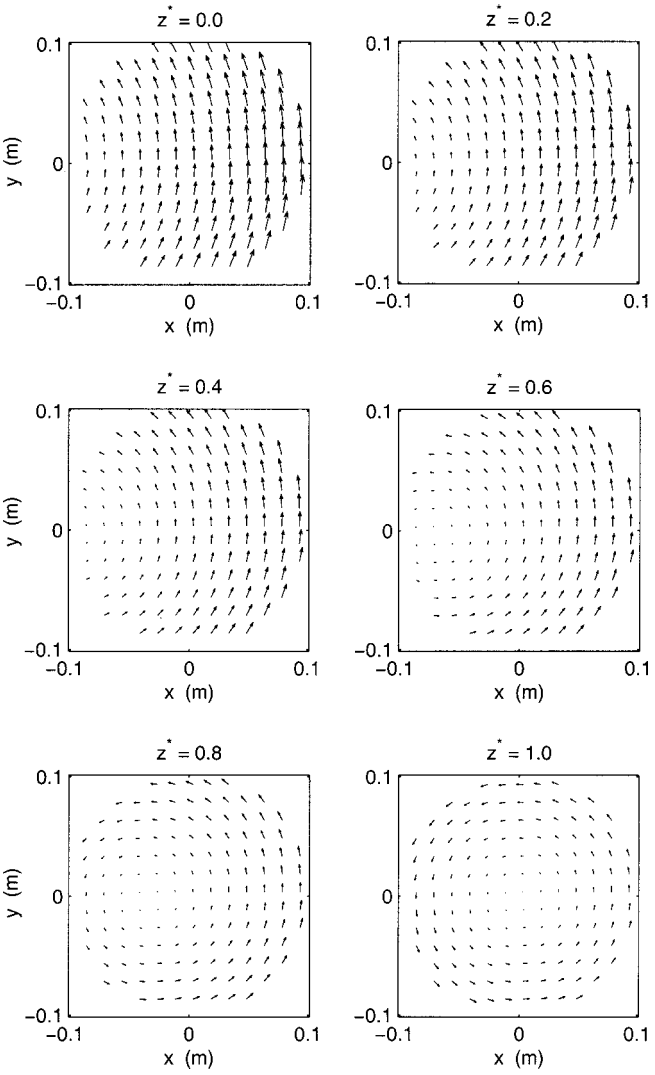

Figure 3. Computed slurry velocity field between pad ($z^* = 0.0$) and wafer ($z^* = 1.0$), where $z^* = z/h(x,y)$. Same input parameters used as in Fig. 2.

The contours of $h(x,y)$ in Fig. 2b show that the wafer tilts down toward the inner (left) edge. The pad velocity at the inner edge is

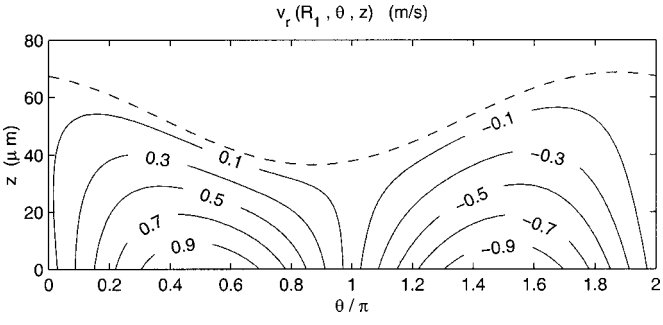

Figure 4. Radial component of slurry velocity at wafer edge, $r = R_1$. Negative contour regions $[v_r(R_1,\theta,z) < 0]$ are slurry inlets, whereas positive regions are outlets. Broken line shows slurry film thickness at wafer edge. Same input parameters used as in Fig. 2.

smaller compared to the outer (right) edge, causing a smaller gap at the inner edge. We also note that the wafer tilts in such a way that the slurry flows through a converging path, thus generating a positive fluid pressure P_f, which supports the applied load. In this case, the computed values for h_0, S_x, and S_y are 43, 15, and -6 μm, respectively. The wafer slope values S_x and S_y, and height h_0 adjust to satisfy the moment and the load constraints. The average slurry film thickness is 48 μm, the maximum film thickness 69 μm, and the minimum thickness h_{min} 36 μm due to tilt of the wafer surface.

Figure 2c shows the computed fluid shear stress distribution at the wafer surface. The fluid shear stress, τ_f, is computed as follows

$$\tau_f(r,\theta) = [\tau_{z\theta}^2(r,\theta,h) + \tau_{zr}^2(r,\theta,h)]^{1/2} \quad [20]$$

where

$$\tau_{z\theta} = -\mu\left[\frac{\partial v_\theta}{\partial z} + \frac{1}{r}\frac{\partial v_z}{\partial \theta}\right] \text{ and } \tau_{zr} = -\mu\left[\frac{\partial v_z}{\partial r} + \frac{\partial v_r}{\partial z}\right] \quad [21]$$

As expected, τ_f at any point on the wafer is approximately inversely proportional to the film thickness h at that point. The fluid shear stress at the wafer surface is the cause of material removal[11-13] in the lubrication regime. Since the wafer rotates about its center, it is useful to average τ_f over θ

$$\tau_{f,avg}(r) = \frac{1}{2\pi}\int_0^{2\pi} \tau_f(r,\theta)d\theta \quad [22]$$

This averaged quantity $\tau_{f,avg}(r)$ is plotted as a function of the wafer radial position r in Fig. 2d. If the removal rate at any r were directly proportional to $\tau_{f,avg}(r)$ alone, then the wafer center would polish 1.2 times faster than would the wafer edge in this case. However, we note that the removal rate depends also on other effects. For example, the wafer edge has easier access to fresh slurry chemicals than the wafer center due to slurry transport limitations, thereby increasing the removal rate at the edge.

Figure 3 shows vector arrow plots of the computed slurry velocity field between the pad and wafer at different normalized heights z^*, where $z^* = z/h$. At the pad ($z^* = 0$) and wafer ($z^* = 1$) surface, the slurry follows the surface velocity of the pad and wafer, respectively, as required by the no-slip conditions. The slurry velocity is composed of pressure- and shear-driven components. These components are represented by the first and second terms, respectively, of Eq. 11. The pad draws in the slurry under the wafer at the bottom edge working against an adverse (positive) pressure gradient as it travels toward the middle. The slurry leaves at the top edge while being accelerated by a negative pressure gradient. The rotating wafer creates a recirculating flow pattern as seen near the left edge for $z^* = 0.6$ and 0.8. The computed 3-D velocity field can be used in mass transport simulations to study convection and diffusion of chemical reactants, products, and abrasive particles in the slurry during CMP. Such a mass transport model is currently under development.

Figure 4 shows the radial component of slurry velocity at the wafer edge $v_r(R_1,\theta,z)$. A negative value indicates that the slurry is drawn toward the center of the wafer. Hence, the slurry enters the region under the wafer where $v_r(R_1,\theta,z) < 0$. Conversely, the slurry outlets are the regions where $v_r(R_1,\theta,z) > 0$. The volumetric flow rate of slurry entering the wafer Q_{in} can be computed by integrating the region where $v_r(R_1,\theta,z) < 0$ as follows

$$Q_{in} = \int_{s(R_1,\theta)}^{h(R_1\theta)}\int_0^{2\pi} v_r(R_1,\theta,z)R_1 d\theta dz \text{ with } v_r < 0 \quad [23]$$

In this case, the computed value of Q_{in} is 358 mL/min. This serves as an estimate for the required slurry delivery rate.

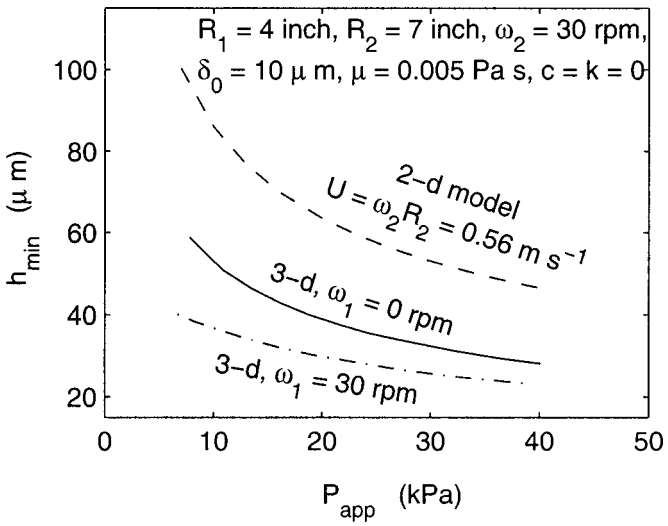

Figure 5. Comparison of 3-D and 2-D lubrication model predictions for minimum film thickness. The 2-D model overpredicts minimum film thickness as it does not take into account the rotations of the wafer and pad.

The regime of CMP operation can be estimated using h_{min}. If h_{min} is greater than the average roughness of the pad surface (~20 μm), then CMP operation is taken to be in the lubrication regime. Conversely, if the computed h_{min} is less than the average roughness of the pad, then the CMP operation is in the contact regime. Hence, h_{min} is an important computed parameter and the effect of the input parameters on h_{min} is studied in detail later in this section. It is noted that the average film thickness could be used instead of h_{min} to estimate the regime of CMP operation; however, h_{min} provides a more conservative estimate for the lubrication regime.

It is instructive to compare the results of the 3-D model to earlier 2-D work to clarify the deficiencies of the latter. The minimum film thickness h_{min} is chosen as the basis of comparison, as it was identified as an important computed parameter which determines the regime of CMP operation. The h_{min} predicted by the present 3-D model is less than half of the value predicted by the 2-D model by Sundararajan *et al.*[13] as shown in Fig. 5. Although qualitative trends are well predicted by the simpler 2-D models, they have several shortcomings. In the 2-D models, the wafer is considered stationary and the pad moves underneath with a linear velocity $U = \omega_2 R_2$. Thus, effects of the rotation of both pad and the wafer are not taken into account by the 2-D formulation. Hence, when the wafer rotation is turned off in the 3-D model, the thickness prediction is closer to the 2-D model (see Fig. 5). It is also noted that in the 3-D model, the h_{min} always occurs near the left edge of the wafer (see Fig. 2b) where the pad has the slowest velocity (approximately 60% smaller than U) resulting in a smaller computed value of h_{min} compared to the 2-D model.

The h_{min} values also were compared with the 3-D model by Runnels and Eyman.[11] They obtain h_{min} values in the range of 63-96 μm for their set of input parameters, while the present 3-D model predicts values between 51-73 μm. Part of the difference in the computed h_{min} values arises from the fact that Runnels and Eyman balance moments in only one direction. When we artificially turned off the y moment balance in our model, the difference in prediction reduced from 25 to 12%. It is not clear what other factors cause the residual difference.

Minimum slurry film dependence on input parameters.—In this section, we present the effects of all input parameters on h_{min}. Figure 6a studies the effect of two of the most important parameters: the applied pressure and wafer and pad speed. In these simulations, the wafer and pad have equal angular velocities. A thicker slurry film is obtained with decrease in P_{app} and/or increase in wafer and

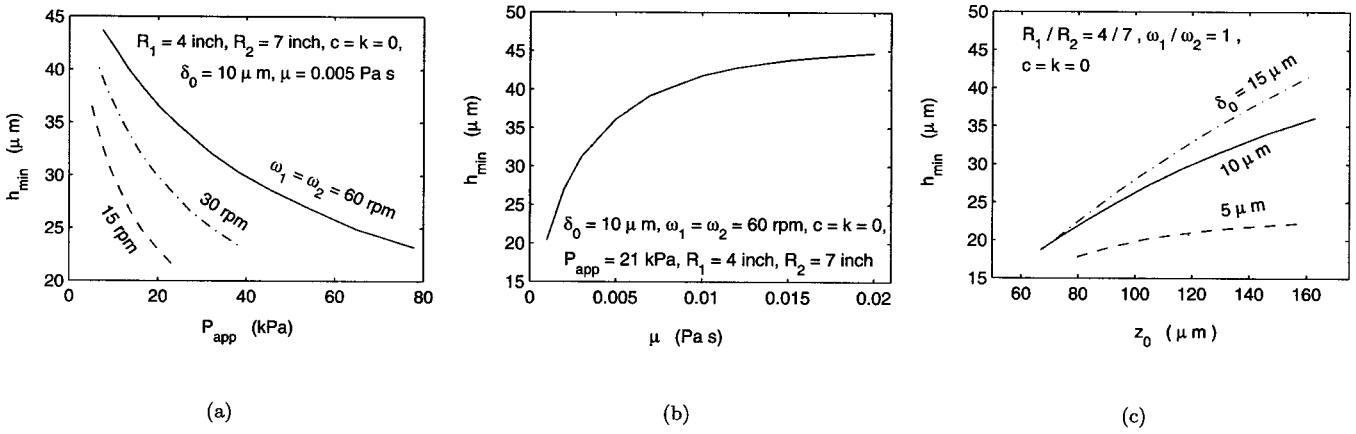

Figure 6. Effect of (a) pressure/speed, (b) slurry viscosity, and (c) z_0 (as defined in Eq. 19) on minimum film thickness.

pad speed. This observation is fairly intuitive from lubrication principles and agrees qualitatively with earlier flow models. Figure 6b shows the effect of viscosity on h_{min}. A more viscous slurry would lead to thicker films. If required, slurry viscosity can be adjusted by additives such as glycerol.[25]

Using dimensional analysis (see Eq. 18), the combined effects of pressure, speed, and viscosity can be represented with a single variable z_0 (as defined in Eq. 19). Figure 6c shows variations of h_{min} with z_0 for a rigid nonporous pad (*i.e.*, $c = k = 0$) and a given wafer curvature, δ_0. Other parameters R_1/R_2, and ω_1/ω_2 have fixed values. Most often, the pad and wafer are rotated at the same speed. Hence, we choose $\omega_1/\omega_2 = 1$, and a value of 4/7 for R_1/R_2 is also typical for CMP tool settings. At a given z_0, a thicker film is obtained with larger δ_0 (for the range studied), but the increase saturates. The effect of δ_0 is studied in detail later in this section.

Figure 7a shows the effect of the angular velocities of wafer and pad on h_{min}. As ω_2 increases, more slurry is drawn under the wafer, resulting in a thicker film. However, h_{min} decreases with increase in wafer speed. This is because the wafer rotation counters the effect of slurry being drawn in by the pad's rotation. Hence, for a given pad speed, we see the maximum h_{min} at zero wafer speed.

Figure 7b shows the effects of wafer curvature and speed on h_{min}. Large curvatures are possible due to stress arising from deposition of multiple metal layers on wafers. A maximum occurs in h_{min}, occurring at a smaller value of δ_0 at a slower speed. As δ_0 increases, a more converging slurry flow path is formed under the wafer, which can support a thicker film; h_0 increases and thus the average film thickness increases with h_{min} also increasing initially. But at the same time as δ_0 increases, the angles of attack also increase to balance the moments. The increase in the angles of attack causes one end of the wafer to dip closer to the pad, thus offsetting the initial increase in h_{min} at high wafer curvatures, as also reported by Runnels and Eyman.[11]

The effect of wafer curvature is further investigated in Fig. 7c which shows a plot of dimensionless h_{min} against δ_0 for different R_1/R_2 and ω_1/ω_2 combinations. As observed earlier (in Fig. 7b), there is a maximum for h_{min}/z_0 which occurs approximately between $0.1 < \delta_0/z_0 < 0.2$ for the given choice of parameters. The film thickness increases when ω_1/ω_2 decreases from 1.0 to 0.8 for a fixed $R_1/R_2 = 0.6$, implying that a decrease in wafer speed relative to pad speed increases h_{min}; this result agrees with the computations presented in Fig. 7a. The effect of wafer radius can be seen while comparing the curves with $R_1/R_2 = 0.6$ and 0.7 at constant $\omega_1/\omega_2 = 1$. An increase in the R_1/R_2 ratio, implying a larger wafer for the same R_2, leads to a decrease in film thickness. Hence, to achieve the same film thickness for a larger wafer we need to increase R_2 such that R_1/R_2 remains constant; thus, larger platen sizes are necessary for larger wafers with conventional CMP tools.

It is noted that a positive δ_0 is necessary for a slurry film to form with the moment constraints being satisfied. This is a drawback of

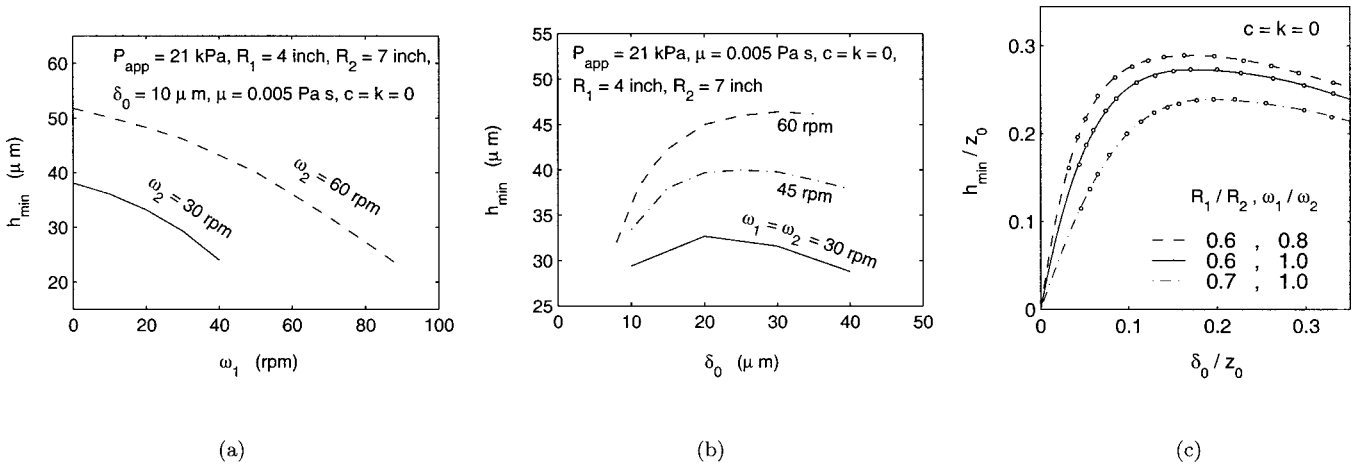

Figure 7. Effect of (a) wafer and pad speed and (b) wafer curvature on minimum film thickness. (c) Plot of dimensionless h_{min} *vs.* dimensionless z_0 (with fits) showing effects of parameters ω_1/ω_2 and R_1/R_2.

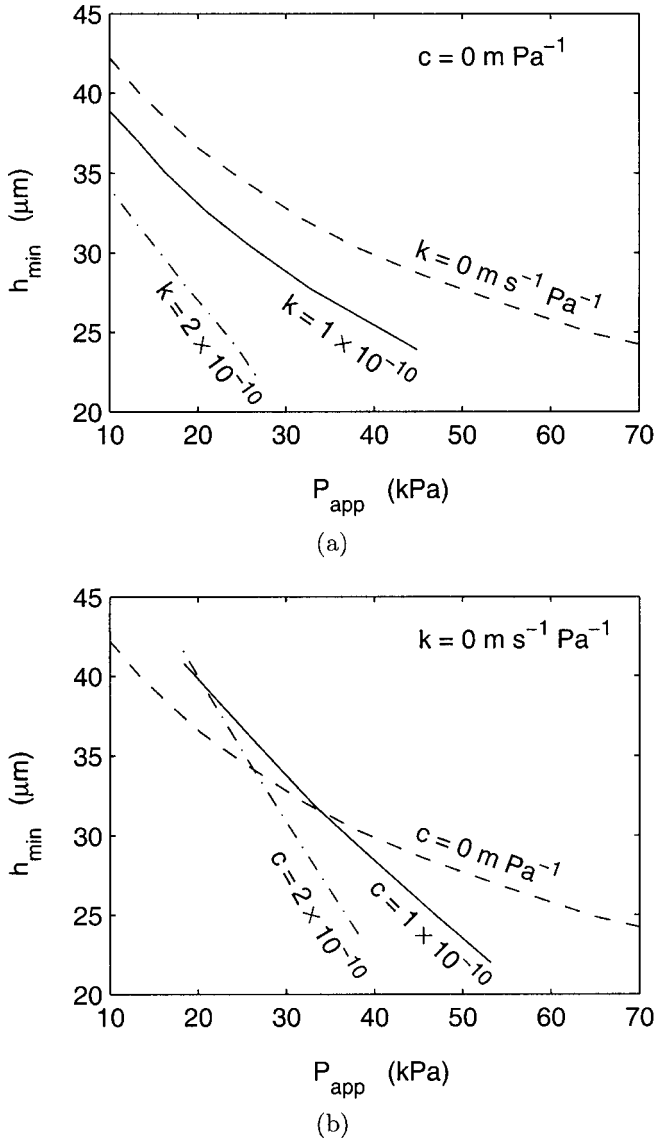

Figure 8. Effect of (a) pad porosity and (b) pad compressibility on minimum film thickness. Input parameters used: $\omega_1 = \omega_2 = 60$ rpm, $R_1 = 4$ in., $R_2 = 7$ in., $\delta_0 = 10$ μm, $\mu = 0.005$ Pa s.

considering complete lubrication, and hints that a contact mechanics model should be consistently included.

All the simulation results described have been for a rigid nonporous pad, *i.e.*, with $c = k = 0$. The effects of pad porosity and compressibility on h_{min} are presented in Fig. 8. Pad porosity causes a certain amount of slurry to seep into the pad thereby reducing the film thickness as seen in Fig. 8a. Figure 8b shows the effect of pad compressibility. Bending of the flexible pad material changes the shape of the wafer/pad gap causing an approximately linear decrease in h_{min} with increasing P_{app}. At lower P_{app}, the bend in the pad adds to the wafer/pad separation resulting in a higher value of h_{min} compared to a rigid pad. However, as P_{app} increases the wafer tilts more (to balance the moments) bringing the top wafer edge closer to the pad, thus reducing h_{min}. So, with a porous and compressible pad one would need a lower P_{app} and/or a higher speed to obtain a thicker slurry film.

Experimental and Results

CMP experiments were performed over a wide range of P_{app} and pad and wafer speed to correlate the measured removal rate and to identify the regimes of CMP operation. 5 in. diam wafers with blanket copper films are polished using an IPEC 372M CMP tool. The diameter of the polishing table is approximately 22.5 in. and the eccentric distance, R_2, between the polishing head and the center of the polishing table is 6.8 in. The pad and wafer are rotated in the same direction at equal speed in all the experiments, *i.e.*, $\omega_1 = \omega_2 = \omega$. When both wafer and pad are rotated at the same rpm ω, the relative velocity between any point on the wafer surface and a corresponding point on the pad surface is the same regardless of the location of the point in question.[2] The relative velocity is then given by $U = \omega R_2$. The applied pressure is varied between 7-42 kPa, while ω ranged from 20 to 80 rpm (which translates to a range of relative velocity U between 0.36 and 1.44 m/s).

Table II. Compositions of slurry 1 and 2.

Slurry label	Active components	Composition
Slurry 1	Potassium ferricyanide	4 wt %
	Ammonium hydroxide	3 vol %
	Alumina particles (0.05 μm diameter)	2.5 wt %
Slurry 2	QCTT1010	30 vol %
	Hydrogen peroxide	10 vol %

Two different slurries are used, labeled slurry 1 and slurry 2, with their active components listed in Table II. Deionized (DI) water is added to the components to make up the slurry. The functions of the individual components of slurry 1 are discussed in Ref. 13. Slurry 2 is a commercial slurry manufactured by Rodel Corp., Newark, Delaware. Slurry 1 is used with two different pads, an IC 1000 pad without any perforations or grooves and a Suba 500 pad; an IC 1400 k-grooved pad is used with slurry 2. Both IC and Suba pads are manufactured by Rodel. The slurry delivery rate is 200 mL/min for all the experiments. The copper removal rate *RR*, is calculated from pre- and post-polish sheet resistance measurements using a four-point probe.

Direct measurement of the slurry film thickness is difficult in the experiments. From the analysis presented in the previous section, we know that the film thickness, for a given pad and constant R_1/R_2 and ω_1/ω_2, is a function of z_0 (see Fig. 6c). In the experiments, R_1/R_2 and ω_1/ω_2 are fixed, and we assume that δ_0 does not vary much from wafer to wafer. For a given pad and slurry, only P_{app} and U are varied in our experiments; hence the slurry film thickness can simply be expressed as a function of $(U/P_{app})^{1/2}$ only. Also, from the simulation results presented in Fig. 6c we know that film thickness increases monotonically with $(U/P_{app})^{1/2}$. The combinations of U and P_{app} for the experiments were chosen to cover a wide range of $(U/P_{app})^{1/2}$.

The normalized copper removal rate RR/U, is plotted against $(U^*/P^*_{app})^{1/2}$ in Fig. 9. The normalized (dimensionless) removal rate, obtained by dividing the measured *RR* by the relative pad velocity U, represents the amount of material removed (in nm) per meter of the pad passing underneath the wafer. The other symbols, U^* and P^*_{app} are dimensionless relative pad speed and applied pressure, respectively and are given by $U^* = U/U_{ref}$ and $P^*_{app} = P_{app}/P_{ref}$, where $U_{ref} = 1$ m/s, and $P_{ref} = 20$ kPa. The x axis of Fig. 9 is a monotonic increasing function of the thickness of slurry film for a given pad-slurry combination. For each pad, the lubrication regime is characterized by the flatter tail of the data, where the slurry film thickness is larger. The contact regime has a steeper slope, which indicates a stronger dependence of RR/U on $(U^*/P^*_{app})^{1/2}$. The Suba 500 and the IC 1400 curves are shifted toward the right compared to that of the IC 1000. This is because a higher U and/or lower P_{app} is needed with a softer pad (Suba 500) and also probably for a grooved pad (IC 1400) for operation in the lubrication regime. A strong correlation between RR/U and $(U^*/P^*_{app})^{1/2}$ is observed for all the pads.

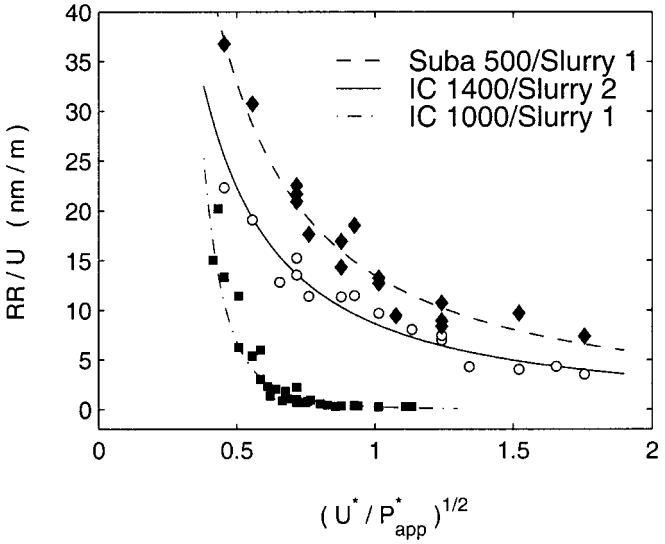

Figure 9. Plot of experimentally measured normalized removal rate against $(U^*/P^*_{app})^{1/2}$. Fits are added to show trends.

We note that the Suba 500 pad has a significantly higher removal rate as compared to the IC 1000 pad for the same slurry, and that this difference cannot be predicted by the effects of compressibility and porosity alone using the available models. There are additional abrasive effects that have not been modeled including pad roughness, pad grooves, partial contact, and particle mechanics; these effects are believed to be important especially for CMP operation near the border between the lubrication and contact regimes.

Conclusions

A 3-D wafer-scale CMP slurry flow model based on lubrication theory was developed using a generalized Reynolds equation derived for arbitrary pad and wafer surface. Pad porosity and compressibility effects are also included in the model. The model predicts slurry film thickness and velocity distributions.

The minimum film thickness determines the degree of contact between the wafer and pad and hence the regime of operation. It is found that a thicker film is more likely to exist at lower P_{app}, higher pad speeds, and lower pad porosity and compressibility. Film thickness shows a maximum with change in wafer curvature. The 3-D model is also compared to earlier 2-D models. The 2-D models overpredict the film thickness as they do not account for wafer and pad rotations and consider flow only in one direction.

The computed 3-D velocity distributions can be used for mass transport models for CMP. The computed velocities also helped in determining slurry inlets and outlets, and in estimating delivery rates.

Dimensional analysis of the Reynolds equation reveals that the film thickness is a monotonic increasing function of $(U/P_{app})^{1/2}$, which correlates well with the normalized removal rates obtained experimentally. The unexpected high removal rate with the Suba 500 pad compared to that of IC 1000 for the same slurry is not clearly understood.

It is possible to extend the model to other polisher configurations such as linear and orbital tools.

Acknowledgments

This work was supported by the Center of Interconnect Science and Technology (CAIST), Semiconductor Research Corporation (SRC) contract no. 98-IC-448. The authors would also like to thank S. Shankar and L. Jiang (Intel Corporation) for helpful discussions.

Two of the authors (W. G. and R. G.) assisted in meeting the publication costs of this article.

References

1. J. M. Steigerwald, S. P. Murarka, and R. J. Gutmann, *Chemical Mechanical Planarization of Microelectronic Materials*, Wiley-Interscience, New York (1997).
2. W. J. Patrick, W. L. Guthrie, C. L. Standley, and P. M. Schiable, *J. Electrochem. Soc.*, **138**, 1778 (1991).
3. S. Sivaram, H. Bath, R. Leggett, A. Maury, K. Monnig, and R. Tolles, *Solid State Technol.*, **35**, 87 (1992).
4. I. Ali, M. Rodder, S. R. Roy, G. Shinn, and M. I. Raja, *J. Electrochem. Soc.*, **142**, 3088 (1995).
5. J. M. Steigerwald, R. Zirpoli, S. P. Murarka, D. Price, and R. J. Gutmann, *J. Electrochem. Soc.*, **141**, 2842 (1994).
6. J. M. Steigerwald, Ph.D. Thesis, Rensselaer Polytechnic Institute, Troy, NY (1995).
7. The *International Technology Roadmap for Semiconductors*, Semiconductor Industry Association, San Jose, CA (1999).
8. G. Nanz and L. E. Camilletti, *IEEE Trans. Semicond. Manuf.*, **8**, 382 (1995).
9. R. S. Subramanian, L. Zhang, and S. V. Babu, *J. Electrochem. Soc.*, **146**, 4263 (1999).
10. D. G. Thakurta, C. L. Borst, D. W. Schwendeman, R. J. Gutmann, and W. N. Gill, *Thin Solid Films*, **366**, 181 (2000).
11. S. R. Runnels and L. M. Eyman, *J. Electrochem. Soc.*, **141**, 1698 (1994).
12. S. R. Runnels, *J. Electrochem. Soc.*, **141**, 1900 (1994).
13. S. Sundararajan, D. G. Thakurta, D. W. Schwendeman, S. P. Murarka, and W. N. Gill, *J. Electrochem. Soc.*, **146**, 761 (1999).
14. C. L. Borst, D. G. Thakurta, W. N. Gill, and R. J. Gutmann, *J. Electrochem. Soc.*, **146**, 4309 (1999).
15. T.-K. Yu, C. C. Yu, and M. Orlowski, *Tech. Dig. Int. Electron Devices Meet.*, , 865 (1993).
16. M. Bhushan, R. Rouse, and J. E. Lukens, *J. Electrochem. Soc.*, **142**, 3845 (1995).
17. D. Stein, D. Hetherington, M. Dugger, and T. Stout, *J. Electron. Mater.*, **25**, 1623 (1996).
18. K. Nakamura, S. Kishii, and Y. Arimoto, *Jpn. J. Appl. Phys.*, **36**, Part 1, No. 3B, 1525 (1997).
19. C. Rogers, J. Coppeta, L. Racz, A. Philipossain, F. B. Kaufman, and D. Bramono, *J. Electron. Mater.*, **27**, 1082 (1998).
20. J. Tichy, J. A. Levert, L. Shan, and S. Danyluk, *J. Electrochem. Soc.*, **146**, 1523 (1999).
21. L. Jiang and S. Shankar, No. 99-ISMIC- in *Proceedings of the 16th International VLSI Multilevel Interconnection Conference* (VMIC), p. 245, Sept 7-9, 1999.
22. N. Patir and H. S. Cheng, *ASME J. Lubr. Technol.*, **100**, 12 (1978).
23. S. R. Runnels and P. Renteln, *Dielectric Sci. Technol.*, **1993**, 110.
24. A. R. Baker, in *Chemical Mechanical Planarization I*, I. Ali. and S. Raghavan, Editors, PV 96-22, p. 228, The Electrochemical Society Proceedings Series, Pennington, NJ (1997).
25. D. M. Permana, Ph.D. Thesis, Rensselaer Polytechnic Institute, Troy, NY (1999).